DOI: 10.1002/ /solr.201900179
Article type: Communication

One-step blade-coated highly efficient nonfullerene organic solar cells with a self-assembled interfacial layer enabled by solvent vapor annealing

Yuanbao Lin, Liyang Yu, Yuxin Xia, Yuliar Firdaus, Sheng Dong, Christian Müller, Olle Inganäs, Fei Huang, Thomas D. Anthopoulos, Fengling Zhang,* and Lintao Hou,**

Y. Lin, Prof. F. Zhang, Prof. L. Hou

Guangdong Provincial Key Laboratory of Optical Fiber Sensing and Communications, Guangzhou Key Laboratory of Vacuum Coating Technologies and New Energy Materials, Guangdong Provincial Engineering Technology Research Center of Vacuum Coating Technologies and New Energy Materials, Siyuan Laboratory, Physics Department, Jinan University, Guangzhou 510632, P.R. China

E-mail: fengling.zhang@liu.se; thlt@jnu.edu.cn

Y. Lin, Dr. Y. Firdaus, Prof. T.D. Anthopoulos

King Abdullah University of Science and Technology (KAUST), KAUST Solar Center (KSC), Thuwal 23955, Saudi Arabia

E-mail: thomas.anthopoulos@kaust.edu.sa

Dr. L. Yu, Prof. C. Müller

Department of Chemistry and Chemical Engineering, Chalmers University of Technology, SE-412 96 Göteborg, Sweden

Dr. Y. Xia, Prof. O. Inganäs, Prof. F. Zhang

Biomolecular and Organic Electronics, Department of Physics, Chemistry and Biology (IFM), SE-581 83, Linköping, Sweden

E-mail: fengling.zhang@liu.se

Dr. S. Dong, Prof. F. Huang

Institute of Polymer Optoelectronic Materials and Devices, State Key Laboratory of Luminescent Materials and Devices, South China University of Technology, Guangzhou 510640, P. R. China

Dr. L. Yu

College of Chemistry, Sichuan University, Chengdu 610064, P. R. China

Keywords: one-step doctor blading; solvent vapor annealing; nonfullerence organic solar cell; self-assembly; interfacial layer

Abstract

A pronounced enhancement of the power conversion efficiency (PCE) by 38% is achieved in one-step doctor-blade printing organic solar cells (OSCs) via a simple solvent vapor annealing (SVA) step. The organic blend composed of a donor polymer, a nonfullerene acceptor and an interfacial layer (IL) molecular component is found to phase-separate vertically when exposed to a solvent vapor-saturated atmosphere. Remarkably, the spontaneous formation of a fine, self-organized IL between the bulk heterojunction (BHJ) layer and the indium tin oxide (ITO) electrode facilitated by SVA, yields solar cells with significantly higher PCE (11.14%) than control devices (8.05%) without SVA and devices (10.06%) made with the more complex two-step doctor-blade printing method. The stratified nature of the ITO/IL/BHJ/cathode is corroborated by a range of complementary characterization techniques including surface energy, cross-sectional scanning electron microscopy, grazing incidence wide angle X-ray scattering and X-ray photoelectron spectroscopy. The present work demonstrates that spontaneously formed IL with SVA treatment, combines simplicity and precision with high device performance, hence making it attractive for large-area manufacturing of next-generation OSCs.

Organic solar cells (OSCs) consisting of bulk-heterojunction (BHJ) nanocomposites have attracted broad interest owing to their facile tunability, simple device structure and low-cost manufacturing via roll-to-roll (R2R) printing technology.[1-4] To date, with the development of nonfullerene (NF) small molecule acceptors, the power conversion efficiency (PCE) values of OSCs have been continuously improving reaching >15% for single-junction cells, and >17% for two-terminal tandem cells.[5-9] However, most of these high-performance OSCs are fabricated via spin-coating–a method not compatible with large-area manufacturing.[10-12] Unlike spin-coating, doctor-blade printing, an alternative and industrial relevant technique, can be employed in both sheet-to-sheet and R2R manufacturing, offering scalability and high-precision control over film thickness and conformity.[13,14] A further advantage of doctor-blade printing technique, that is particularly relevant to research on new materials, is that it requires a low amount of materials without affecting the device performance.[15,16]

Recently, PCEs of >10% have been reported for doctor-bladed NF-based OSCs.[17-19] Key to this success is the use of interfacial layers (ILs) as they enable optimization of the fill factor (FF) and open circuit voltage (V_{OC}) by reducing the energy barrier for carrier extraction through the formation of interfacial dipoles.[20-23] However, ILs such as poly [(9,9-bis(3′-(N,N-dimethylamino)propyl)-2,7-fluorene)-alt-2,7-(9,9-dioctylfluorene)] (PFN) and zinc oxide (ZnO) are mostly processed by spin-coating, which is incompatible with large-area R2R processing. On the other hand, printing of ultrathin ILs (<10 nm) often leads to coarse layers with high root mean square (RMS) surface roughness, which in turn decreases device performance due to the inhomogeneity of film thickness and sub-optimal carrier extraction.[24,25] Thus, an alternative process for the deposition of high quality ILs is required for next-generation printed OSCs.

Spontaneous segregation (self-assembly) is one process that has previously been exploited for the formation of ILs during spin coating of BHJ layer.[26] Using this approach,

high PCE values of >10% were obtained in spin-coated OSCs with a self-organized IL, owing to efficient charge extraction.[27-29] Unfortunately, OSCs produced via one-step printing methods exhibit low PCE that is typically <10%, due to the inability to independently optimize the BHJ morphology and IL formation during drying.[30] For example, optimized phase separation of the BHJ components is often achieved at temperatures >60 °C for one-step printed fullerene-based OSCs. However, this relatively high-temperature step has adverse effects on the homogeneity of the spontaneously formed IL due to the short drying time which suppresses self-stratification.[29,30] Thus, novel methods are needed to obtain simultaneously optimized BHJ and IL morphologies in one-step printed OSCs.

Here, we develop a facile method of solvent vapor annealing (SVA) to manipulate one-step printed BHJ:IL nanocomposites for the first time. One of the highest PCE of 11.14% is achieved for SVA treated NF-based OSCs composed of the poly[(2,6-(4,8-bis(5-(2-ethylhexyl)thiophen-2-yl)benzo[1,2-b:4,5-b']dithiophene)-*co*-(1,3-di(5-thiophene-2-yl)-5,7-bis(2-ethylhexyl)-benzo[1,2-c:4,5-c']dithiophene-4,8-dione)] (PBDB-T) as the donor, and IT-M as the acceptor blended with the PFN acting as the IL material. The PCE of SVA-treated OSCs based on these materials combination is 38% higher (11.14%) than the value measured for one-step deposited cells without the SVA step (8.05%). Importantly, the one-step printed NF-based OSCs subjected to SVA also exhibit higher performance when compared to control cells processed via the more complex two-step sequentially printed PFN and BHJ; an effect attributed to the self-organized nature of the PFN IL and the lower surface roughness as compared to the blade-coated PFN layer. Our results show that spontaneous formation of the IL, aided by the SVA step, can eliminate performance deterioration without compromising device/system manufacturability. The chemical structures of electron donor PBDB-T, NF acceptor IT-M and electron extraction layer PFN are shown in **Figure 1**a. The process steps for one-step (Type-I) and two-step (Type-II) doctor-blade printing deposition and the resulting device architecture, are schematically depicted in Figure 1b. For one-step doctor-

blade printing OSCs, the solution of PFN:BHJ nanocomposites is directly blade coated on top of the indium tin oxide (ITO)-coated electrode at different substrate temperature and PFN concentration. After the mixtures of PFN:BHJ films are blade-coated (Figure 1c), the samples were directly placed into a Petri dish filled with chlorobenzene (CB) solution on a hot plate maintained at 70 °C. The PFN molecules would form a complete IL via vertical spontaneous phase separation during SVA. The corresponding current density-voltage (*J*–*V*) characteristics measured for devices prepared under different processing conditions are presented in Figures. S1 and S2, with the key cell parameters summarized in Tables S1 and S2. As can be seen, the V_{OC} drops gradually when the substrate temperature during SVA treatment increases from 25 to 85 ˚C. The highest PCE value of 8.93% is obtained for cells prepared at ≈ 40 ˚C exhibiting a V_{OC} of 0.91 V, a short-circuit current density (J_{SC}) of 16.1 mA/cm^2, and a FF of 0.61. Interestingly, the PCE for cells processed at >40 ˚C decreases with increasing substrate temperature, an effect ascribed to fast drying of the bilayer which forbids the formation of a continuous and uniform PFN interlayer.[30]

In an effort to prolong the drying time of the mixed layer, a SVA step was employed directly after doctor-blade printing. The duration of the SVA step was varied from 0 to 45 min (Figure S3 and Table S3) for doctor-blade coated films maintained at 70 ˚C, since this particular NF-based BHJ system exhibits optimal morphology at higher annealing temperatures.[31,32] The optimum SVA duration is found to be 30 min for this particular system. Impressively, a combination of SVA with the one-step doctor-blade printing yields Type-I devices with a remarkably high PCE of 11.14%, a direct result of the high J_{SC} of 17.05 mA/cm^2, a high V_{OC} of 0.94 V and a high FF of 0.69. The PCE of one-step printing Type-I device with SVA treatment is 38% higher than 8.05% of Type-I device without SVA. To the best of our knowledge, the obtained PCE value of >11% is one of the highest values reported to date for one-step printed OSCs featuring a self-assembled IL.[27,30,33] For comparison, two-step doctor-blade printing OSC were also produced with varying PFN thickness, substrate

temperature as well as SVA treatment (Figure S4-6, Table S4-6). A maximum PCE value of 10.06% was obtained for Type-II cells with a J_{SC} of 16.58 mA/cm^2, a FF of 0.64 and a similarly high V_{OC} of 0.94 V. These results demonstrate the attractiveness of SVA in combination with the one-step printing method for R2R manufacturing. The external quantum efficiency (EQE) spectra of the PBDB-T:IT-M-based devices are shown in **Figure 2**b. All cells show strong photo response in the range 350-750 nm, which is consistent with the absorption spectra of the blend films (Figure S7). Moreover, the integral current density values deduced from EQE spectra match well with those obtained from the *J-V* measurements (Table 1). The PCEs of one-step fullerene/non-fullerene OSCs fabricated by doctor blade in previous reports are presented in Figure 2c.[27,30,33] It can be seen that our one-step doctor-bladed OSCs with a conventional nonfullerene system show the very high PCEs among the reported results, due to the optimized electrical property of IL through SVA.

To understand the reason behind the PCE enhancement upon SVA treatment of the doctor-bladed OSCs, a systematic investigation of the BHJ morphology was carried out. Firstly, the top and bottom surface molecular allocations in PFN:BHJ were analyzed by measuring the physicochemical properties.[19,34] Surface energies of blend films were measured based on Owens equation (see Tables S7 and S8 and details therein).[35] As shown in Figure S8, the surface energy of PFN layer (48.2 mN/m) is much higher than that of the donor-acceptor BHJ film (22 mN/m) and close to that of ITO (51.1 mN/m). Due to high surface energies of both ITO and PFN layers, the PFN molecules in PFN:BHJ film are expected to migrate towards the surface of the ITO electrode in order to minimize the bulk free energy while spontaneously forming the IL while drying.[26,29] With the aid of an adhesive tape, we were able to delaminate the printed PFN:BHJ layer from the ITO electrode (see *Experimental Section*),[36] and study its surface energy and chemical composition as a function of processing conditions.

When the PFN:BHJ layer is blade coated at high temperature, some amount of the PFN remains on the top surface of the BHJ layer because of the short drying time, leading to slightly higher surface energy (30.7 mN/m). Interestingly, following SVA treatment, the surface energy of the BHJ decreases to 22.5 mN/m, a value very similar to that of pristine BHJ layer. At the same time, the surface energy of the bottom layer, measured after been peeled-off,[36] rises rapidly to 45.7 mN/m and approaches that of pure PFN layer. Thus, the results obtained so far indicate that doctor-bladed blends of PFN:BHJ tend to self-organize into an IL between BHJ and the ITO electrode. Deposition of the PFN:BHJ ink at higher temperatures (>60 °C) results to incomplete IL formation and to suboptimal device performance. Using the post-deposition SVA step helps to minimize the latter effect leading to remarkable PCE improvements by 38% (Figure 2a).

To further analyze the vertical distribution of the different materials components, cross-sectional scanning electron microscopy (SEM) was utilized (**Figure 3**a-b). In Type-I layers (i.e. no SVA) we observe the presence of many small granular aggregates approximately 5 nm in diameter (Figure 3a). It should be attributed these to trace amounts of PFN molecules remaining present within the BHJ layer after processing.[26, 30] In contrast, SVA treatment of the PFN:BHJ blend layers leads to a clear formation of a self-organized PFN IL between the BHJ and the ITO electrode (Figure 3b). This observation is consistent with the increased surface energy of the bottom PFN:BHJ interface which approaches that of the pristine PFN layer. The cross-sectional SEM image in Figure 3b is similar to that of two-step Type-II cells shown in Figure 3c. However, it can be argued that the self-assembled PFN IL in Figure 3b appears to be smoother than the sequentially blade-coated PFN layer in Figure 3c. This feature may well be the reason for the higher FF and better device performance achieved (Figure 2 and Table 1).

In an effort to determine the elemental composition of the BHJ layers at the interfaces, X-ray photoelectron spectroscopy (XPS) was employed. Figure 3d shows the high-resolution

XPS spectra of S 2p intensity of the bottom and top surface of several BHJ films and a neat PFN layer prepared at different conditions. Since PFN does not contain any sulfur, any measured S 2p signal can safely be attributed to the presence of the PBDB-T and/or IT-M molecules on that particular interface, whilst its absence/suppression would signify the presence of PFN at that particular interface. Interestingly, the strong S 2p signal detected for the PFN:BHJ film without SVA (Figure 3d), suggests that the phase separation and PFN IL formation is incomplete and most likely responsible for the low device performance seen in Figure 2a. Analysis of the top interface (Figure 3e), on the other hand, yields a strong S 2p signal for all blend layers, indicating that PFN migrates to the bottom interface and/or remains within the bulk of the BHJ layer in agreement with Figure 3a-c.

Further analysis of the BHJ microstructure was performed using transmission electron microscopy (TEM). The TEM image of as-coated PFN:BHJ layer in Figure S9a indicates the presence of large aggregates. Application of the SVA step (Figure S9b), results to PFN:BHJ layers with a more refined fibril network morphology, suggesting that fibrils act as efficient conduits for the charge carrier transport. The Type-II (PFN/BHJ) film shows quite similar internal phase morphology compared to the Type-I layer (PFN:BHJ) with SVA, in agreement with the cross-sectional SEM data (Figure 3a-c). Furthermore, we performed atomic force microscopy (AFM) measurements to investigate the surface morphology of the different films (**Figure 4**). The PFN:BHJ blend film without SVA exhibits crater-like features while the PFN:BHJ film subjected to SVA appears smoother with a well-distributed phase separation just like Type-II layers. These remarkably different surface topographies are reflected in the different root-mean-square (RMS) of the surface roughness which for Type-I reduces rapidly from 5.24 to 1.83 nm upon SVA treatment. Surprisingly, the latter RMS value is even lower than that of Type-II film (2.07 nm). The measured surface RMS values are in qualitative agreement with the cross-sectional SEM images in Figure 3a-c, where differences in the flatness of each layer can easily be observed. To this end, we note that the RMS roughness

value of the sequentially deposited PFN film is higher than the self-assembly PFN IL after SVA (Figure S8d-e). This key feature is the most likely reason for the rougher interface seen in Type-II layers Figure 4c). We thus hypothesize that in the present type of OSCs, the smoother interface benefits the overall device operation leading to higher FF, less recombination and eventually higher PCE (Figure 2).

In order to identify any possible relationship between the higher device performance and molecular packing within the donor-acceptor BHJ, the doctor-bladed films were studied using the grazing incidence wide angle X-ray scattering (GIWAXS) technique (**Figure 5**). Both the donor and acceptor materials exhibit relatively similar lamellar stacking distance (q) of 2.88 and 3.14 nm^{-1}, respectively. Interestingly, the neat PBDB-T molecules are found predominately edge-on with its lamellar diffraction along the meridian whilst the neat IT-M molecules prefer to be face-on with its π stacking diffraction found along the meridian (Figure S10). We quantified these configurational anisotropies by calculating the Herman's Orientation Factor[37] (f) from the azimuthal distribution of these two diffraction peaks. The value of f ranges from 0 to 1 corresponding to fully isotropic to fully anisotropic. Our calculations yielded f value of 0.58 for PBDB-T suggesting a strong anisotropy with some molecules oriented isotopically and 0.77 for the IT-M indicating that most of the molecules are aligned. Following the SVA treatment, the signal intensity increases significantly for both lamellar and π stacking diffraction of the IT-M component within the Type-I layers, suggesting an increase of the acceptor crystallinity as shown in Figure 5d. Interestingly, Type-II layers display a very similar diffraction pattern to Type-I films after SVA but with a slightly lower lamellar diffraction intensity. This apparent lower degree of crystallinity may well be one of the reasons for the lower device performance observed for Type-II cells.

The charge carrier transport within the various layers was further investigated via J–V analysis in the dark (Figure S11). Evidently, the Type-I devices without SVA treatment show a high leakage current under reverse bias direction. However, the cells that have undergone

the SVA treatment exhibit better diode characteristics with a lower reverse current. Reducing the reverse leakage current is critical as it is known to increase the FF and *V*oc in OSCs.[38] Since the relatively rougher nature of the two-step blade coated Type-II cells lead to slightly higher reverse currents (as compared to Type-I cells following SVA treatment), the FF of the cell decreases accordingly.

Finally, the nature of the charge-transfer (CT) state was investigated using Fourier transform photocurrent spectroscopy (FTPS). Figure S12 shows the CT region of EQE spectra and the corresponding theoretical fittings of the CT band using:

$$EQE_{CT}(E) = \frac{f}{E\sqrt{4k\pi\lambda T}} exp\left(\frac{-(E_{CT}+\lambda-E)^2}{4k\pi\lambda T}\right) \quad (1)$$

where, k is the Boltzmann's constant, T is the absolute temperature, f is a prefactor, E_{CT} is the energy of the CT states, and λ is the reorganization energy associated with the CT absorption process.[39] The E_{CT} values calculated for the various cells are 1.54 and 1.48 eV for Type-I samples w/o SVA, respectively. The difference of 0.06 eV in the two E_{CT} values is consistent with the difference in V_{OC} between the two devices. Interestingly, the E_{CT} and V_{OC} are in good agreement with the empirical relation of $V_{OC} = E_{CT}/q - 0.6$.[40] The E_{CT} value of the Type-I device with SVA, on the other hand, is similar to that of Type-II cells, indicating that the conformal and uniform nature of the self-forming PFN interface layer in Type-I device following SVA treatment is responsible for the increased E_{CT} and V_{OC}. Moreover, for Type-I device with SVA, the λ value of 0.20 eV is obtained from the fitting in Figure S11, which is lower than 0.23 eV for Type-II device, and 0.28 eV for Type-I cells without SVA, indicating the tremendously beneficial role of the SVA treatment step.

In conclusion, we have demonstrated that the PCE of one-step blade-coated NF-based OSCs can be increased from 8.05% to 11.14% with the introduction of a self-formed PFN-based interfacial layer between the active donor-acceptor BHJ and the ITO electrode. The

high-quality IL can be formed by exposing the blade-coated blend IL:BHJ layer to a saturated solvent atmosphere. The maximum PCE achieved for the SVA-treated cells is 11.14% and represents one of the highest values to date for OSCs based on spontaneously formed ILs. Importantly, the one-step blade-coated devices subjected to SVA exhibit superior performance to traditional, and more complex, two-step coated OSCs (10.06%) mainly owing to smoother nature of the self-forming PFN IL as confirmed by complementary analytical techniques including AFM, SEM, TEM and GIWAXS. The present work demonstrates an alternative route towards simplified manufacturing of high-performance OSCs.

Experimental Section

Materials: PBDB-T (M_n=12.1kDa, M_w=21.9kDa, PDI=1.81) and IT-M were purchased from Solarmer Materials Inc. The PFN solution used to make the cathode buffer layers is synthesized in our lab. PFN was dissolved in methanol (with a few drops of acetic acid to ionize PFN) with a concentration of 1 mg/mL for two-step devices, while PFN was dissolved in CB:DIO (99:1 by volume) solution with a concentration of 17 mg/mL for mixing with PBDB-T:IT-M active solution. For the PBDB-T:IT-M active solution, the blending ratio of PBDB-T:IT-M is 1:1 with a concentration of 17 mg/mL in a solvent system CB:DIO (99:1 by volume). For the PFN:PBDB-T:IT-M nanocomposite solution, 4 wt% of PFN from CB:DIO solution is doped into the PBDB-T:IT-M active solution.

Devices fabrication: The glass substrates were cleaned with alkaline lotion, deionized water, acetone and isopropanol in that order. For the reference two-step coating device with the structure of ITO/PFN/BHJ/MoO_3/Ag, a 10-nm-thick PFN layer is firstly doctor bladed from methanol on top of the clean ITO substrate with the 10 μm gap height of the doctor blade and a 30 mm/s printing speed. Then the PBDB-T:IT-M active layer is doctor-bladed on top of the PFN layer with the substrate temperature of 70 °C, the 20 μm gap height of the doctor blade and a 40 mm/s printing speed. For one-step printing devices with the structure of

ITO/PFN:BHJ/MoO_3/Ag, the PFN:PBDB-T:IT-M solution is doctor-bladed directly on top of the clean ITO. Finally, 10-nm-thick MoO_3 and 100-nm-thick Ag are thermally evaporated under a pressure of 2×10^{-4} Pa onto the BHJ films, respectively. To expose the bottom contact property, the blend films were peeled off with the adhersive Kapton tape by hand.

Measurements and characterization: The current *J-V* characteristics are measured using a Keithley 2400 source meter under illumination of an AM 1.5G solar simulator with an intensity of 100 mW/cm^2 (Sun 2000 Solar Simulator, Abet Technologies, Inc.). The EQE data are recorded with a QE-R test system from Enli Technology Company (Taiwan). The film thickness is measured by using a surface profiler (XP-2). The nanoscale morphology of blend films is observed by using AFM in scanAsyst mode (Bioscope Catylyst Nanoscope-V produced by Bruker in USA) and TEM (PHILIPS TECNAI-10). The cross-sectional image is measured by SEM (ULTRA55, Zeiss). Contact angles using water and formamide as the testing liquids are obtained with a drop shape analyzer DSA100 instrument. X-ray photoelectron spectroscopy (K-ALPHA+, Thermo Fisher Scientific) with AlKα X-rays (1486.69 eV) is used to determine the chemical composition of PFN and BHJ films. The beam spot size is 400 μm and energy step size is 0.1eV/step. The highly sensitive FTPS data are obtained using a Vertex 70 from Bruker optics. Grazing-incidence wide-angle X-ray scattering (GIWAXS) measurements are performed at the D-line, Cornell High Energy Synchrotron Source (CHESS) at Cornell University. The X-ray beam with a wavelength of 1.162 Å is directed onto the samples at an incident angle of 0.15°. A Pilatus 200k detector located 177.2 mm from the sample is used with an exposure time of 3 s.

Supporting Information

Supporting Information is available from the Wiley Online Library or from the author.

Acknowledgements

The authors are grateful to the NSFC Project (61774077, 61274062, 11204106), the Guangzhou Science and Technology Plan Project (201804010295), the Research and Development Program in Key Areas of Guangdong Province (2019B090921002) and the Fundamental Research Funds for the Central Universities for financial support. L.T. acknowledges the support from Sunflare Institute of Solar Energy, Jinan University. F.Z. acknowledges the Swedish Government Research Area in Materials Science on Functional Materials at Linköping University (Faculty Grant SFO-Mat-LiU No. 200900971) and the collaboration between Linköping University and Jinan University supported by Jinan University. T.D.A., Y.L. and Y.F. acknowledges the financial support from King Abdullah University of Science and Technology (KAUST). C.M. and F.Z. acknowledge financial support from the Knut and Alice Wallenberg Foundation through the project "Mastering Morphology for Solution-borne Electronics". L. Y. and C. M. thank Cornell High Energy Synchrotron Source (CHESS, supported by the National Science Foundation under award DMR-1332208) for providing the experiment time for the GIWAXS measurements.

Received: ((will be filled in by the editorial staff))

Revised: ((will be filled in by the editorial staff))

Published online: ((will be filled in by the editorial staff))

References

[1] Z. C. He, C. M. Zhong, S. J. Su, M. Xu, H. B. Wu, Y. Cao, *Nat. Photonics* **2012**, 6, 591.

[2] R. Sondergaard, M. Hosel, D. Angmo, T. T. Larsen-Olsen, F. C. Krebs, *Mater. Today* **2012**, 15, 36.

[3] a) N. Espinosa, M. Hösel, D. Angmo, F. C. Krebs, *Energ. Environ. Sci* **2012**, 5, 5117; b) S. Li, L. Ye, W. Zhao, S. Zhang, S. Mukherjee, H. Ade, J. Hou, *Adv. Mater.* **2016**,

28, 9423.

[4] C. J. M. Emmott, N. J. Ekins-Daukes, J. Nelson, *Energ. Environ. Sci* **2014**, 7, 1810.

[5] Z. Xiao, X. Jia, L. Ding, *Sci. Bull* **2017**, 62, 1562.

[6] L. Meng, Y. Zhang, X. Wan, C. Li, X. Zhang, Y. Wang, X. Ke, Z. Xiao, L. Ding, R. Xia, H.-L. Yip, Y. Cao, Y. Chen, *Science* **2018**, 6407, 1094.

[7] Z. Zhou, S. Xu, J. Song, Y. Jin, Q. Yue, Y. Qian, F. Liu, F. Zhang, X. Zhu, *Nat. Energy* **2018**, 3, 952.

[8] J. Yuan, Y. Zhang, L. Zhou, G. Zhang, H.-L. Yip, T.-K. Lau, X. Lu, C. Zhu, H. Peng, P. A. Johnson, M. Leclerc, Y. Cao, J. Ulanski, Y. Li, Y. Zou, *Joule* **2019**, DOI: 10.1016/j.joule.2019.01.004.

[9] Y. Cui, H. Yao, L. Hong, T. Zhang, Y. Xu, K. Xian, B. Gao, J. Qin, J. Zhang, Z. Wei, J. Hou, *Adv Mater* **2019**, DOI: 10.1002/adma.201808356e1808356.

[10] F. C. Krebs, N. Espinosa, M. Hösel, R. R. Søndergaard, M. Jørgensen, *Adv. Mater.* **2014**, 26, 29.

[11] M. Jørgensen, J. E. Carlé, R. R. Søndergaard, M. Lauritzen, N. A. Dagnæs-Hansen, S. L. Byskov, T. R. Andersen, T. T. Larsen-Olsen, A. P. L. Böttiger, B. Andreasen, L. Fu, L. Zuo, Y. Liu, E. Bundgaard, X. Zhan, H. Chen, F. C. Krebs, *Sol. Energ. Mat. Sol. C.* **2013**, 119, 84.

[12] E. Bundgaard, F. Livi, O. Hagemann, J. E. Carlé, M. Helgesen, I. M. Heckler, N. K. Zawacka, D. Angmo, T. T. Larsen-Olsen, G. A. dos Reis Benatto, B. Roth, M. V. Madsen, M. R. Andersson, M. Jørgensen, R. R. Søndergaard, F. C. Krebs, *Adv. Energy Mater.* **2015**, 5, 1402186.

[13] Y. Firdaus, V. M. Le Corre, J. I. Khan, Z. Kan, F. Laquai, P. M. Beaujuge,T. D. Anthopoulos, *Adv. Sci.*, **2019**, 1802028.

[14] D. Vak, K. Hwang, A. Faulks, Y.-S. Jung, N. Clark, D.-Y. Kim, G. J. Wilson, S. E. Watkins, *Adv. Energy Mater.* **2015**, 5, 1401539.

[15] a) F. C. Krebs, S. A. Gevorgyan, J. Alstrup, *J. Mater. Chem.* **2009**, 19, 5442; b) L. Ye, Y. Xiong, H. Yao, A. Gadisa, H. Zhang, S. Li, M. Ghasemi, N. Balar, A. Hunt, B. T. O'Connor, J. Hou, H. Ade, *Chem. Mater.* **2016**, 28, 7451.

[16] a) M. Helgesen, J. E. Carlé, G. A. dos Reis Benatto, R. R. Søndergaard, M. Jørgensen, E. Bundgaard, F. C. Krebs, *Adv. Energy Mater.* **2015**, 5, 1401996; b) L. Ye, Y. Xiong, S. Li, M. Ghasemi, N. Balar, J. Turner, A. Gadisa, J. Hou, B. T. O'Connor, H. Ade, *Adv. Funct. Mater.* **2017**, 27, 1702016.

[17] W. Zhao, S. Zhang, Y. Zhang, S. Li, X. Liu, C. He, Z. Zheng, J. Hou, *Adv. Mater.* **2018**, 30, 1704837.

[18] L. Ye, Y. Xiong, Q. Zhang, S. Li, C. Wang, Z. Jiang, J. Hou, W. You, H. Ade, *Adv Mater* **2018**, 30, 1705485.

[19] Y. Lin, Y. Jin, S. Dong, W. Zheng, J. Yang, A. Liu, F. Liu, Y. Jiang, T. P. Russell, F. Zhang, F. Huang, L. Hou, *Adv. Energy Mater.* **2018**, 13, 1701942.

[20] S. Braun, W. R. Salaneck, M. Fahlman, *Adv. Mater.* **2009**, 21, 1450.

[21] Z.-G. Zhang, B. Qi, Z. Jin, D. Chi, Z. Qi, Y. Li, J. Wang, *Energ. Environ. Sci.* **2014**, 7, 1966.

[22] Z. Zheng, Q. Hu, S. Zhang, D. Zhang, J. Wang, S. Xie, R. Wang, Y. Qin, W. Li, L. Hong, N. Liang, F. Liu, Y. Zhang, Z. Wei, Z. Tang, T. P. Russell, J. Hou, H. Zhou, *Adv. Mater.* **2018**, 34, 1801801.

[23] F. Zhang, M. Ceder, O. Inganäs, *Adv. Mater.* **2007**, 19, 1835.

[24] P. Cheng, H. Bai, N. K. Zawacka, T. R. Andersen, W. Liu, E. Bundgaard, M. Jørgensen, H. Chen, F. C. Krebs, X. Zhan, *Adv. Sci.* **2015**, 2, 1500096.

[25] D. Angmo, T. R. Andersen, J. J. Bentzen, M. Helgesen, R. R. Søndergaard, M. Jørgensen, J. E. Carlé, E. Bundgaard, F. C. Krebs, *Adv. Funct. Mater.* **2015**, 25, 4539.

[26] a) Z. Peng, Y. Zhang, Y. Xia, K. Xiong, C. Cai, L. Xia, Z. Hu, K. Zhang, F. Huang, L. Hou, *J. Mater. Chem. A* **2015**, 3, 20500. b) L. Ye, W. Zhao, S. Li, S. Mukherjee, J. H.

Carpenter, O. Awartani, X. Jiao, J. Hou, Harald Ade, *Adv. Energy Mater.* **2017**, 7, 1602000.

[27] B. Yang, S. Zhang, S. Li, H. Yao, W. Li, J. Hou, *Adv. Mater.* **2019**, 31, 1804657.

[28] N. Zheng, Z. Wang, K. Zhang, Y. Li, F. Huang, Y. Cao, *J. Mater. Chem. A* **2019**, 7, 1429.

[29] J. Vinokur, B. Shamieh, I. Deckman, A. Singhal, G. L. Frey, *Chem. Mater.* **2016**, 28, 8851.

[30] Y. Lin, C. Cai, Y. Zhang, W. Zheng, J. Yang, E. Wang, L. Hou, *J. Mater. Chem. A* **2017**, 5, 4093.

[31] Z. Li, W. Zhang, X. Xu, Z. Genene, D. Di Carlo Rasi, W. Mammo, A. Yartsev, M. R. Andersson, R. A. J. Janssen, E. Wang, *Adv. Energy Mater.* **2017**, 14, 1602722.

[32] Y. Lin, S. Dong, Z. Li, W. Zheng, J. Yang, A. Liu, W. Cai, F. Liu, Y. Jiang, T. P. Russell, F. Huang, E. Wang, L. Hou, *Nano Energy* **2018**, 46, 428.

[33] S. Kim, H. Kang, S. Hong, J. Lee, S. Lee, B. Park, J. Kim, K. Lee, *Adv. Funct. Mater.* **2016**, 26, 3563.

[34] H. Kang, S. Kee, K. Yu, J. Lee, G. Kim, J. Kim, J. R. Kim, J. Kong, K. Lee, *Adv. Mater.* **2015**, 27, 1408.

[35] D. K. Owens, Richmond, Virginia, R. C. Wendt, *J. Appl. Polym. Sci.* **1969**, 13, 1741.

[36] H. Zhang, W.-Y. Tan, S. Fladischer, L. Ke, T. Ameri, N. Li, M. Turbiez, E. Spiecker, X.-H. Zhu, Y. Cao, C. J. Brabec, *J. Mater. Chem. A* **2016**, 4, 5032.

[37] J. Hermans, P. Hermans, D. Vermaas, A. Weidinger, *Recueil des Travaux Chimiques des Pays‐Bas* **1946**, 65, 427.

[38] N. Li, J. D. Perea, T. Kassar, M. Richter, T. Heumueller, G. J. Matt, Y. Hou, N. S. Guldal, H. Chen, S. Chen, S. Langner, M. Berlinghof, T. Unruh, C. J. Brabec, *Nat. Commun.* **2017**, 8, 14541.

[39] K. R. Graham, C. Cabanetos, J. P. Jahnke, M. N. Idso, A. El Labban, G. O. Ngongang

Ndjawa, T. Heumueller, K. Vandewal, A. Salleo, B. F. Chmelka, A. Amassian, P. M. Beaujuge, M. D. McGehee, *J. Am. Chem. Soc.* **2014**, 136, 9608.

[40] W. Zhao, D. Qian, S. Zhang, S. Li, O. Inganas, F. Gao, J. Hou, *Adv. Mater.* **2016**, 28, 4734.

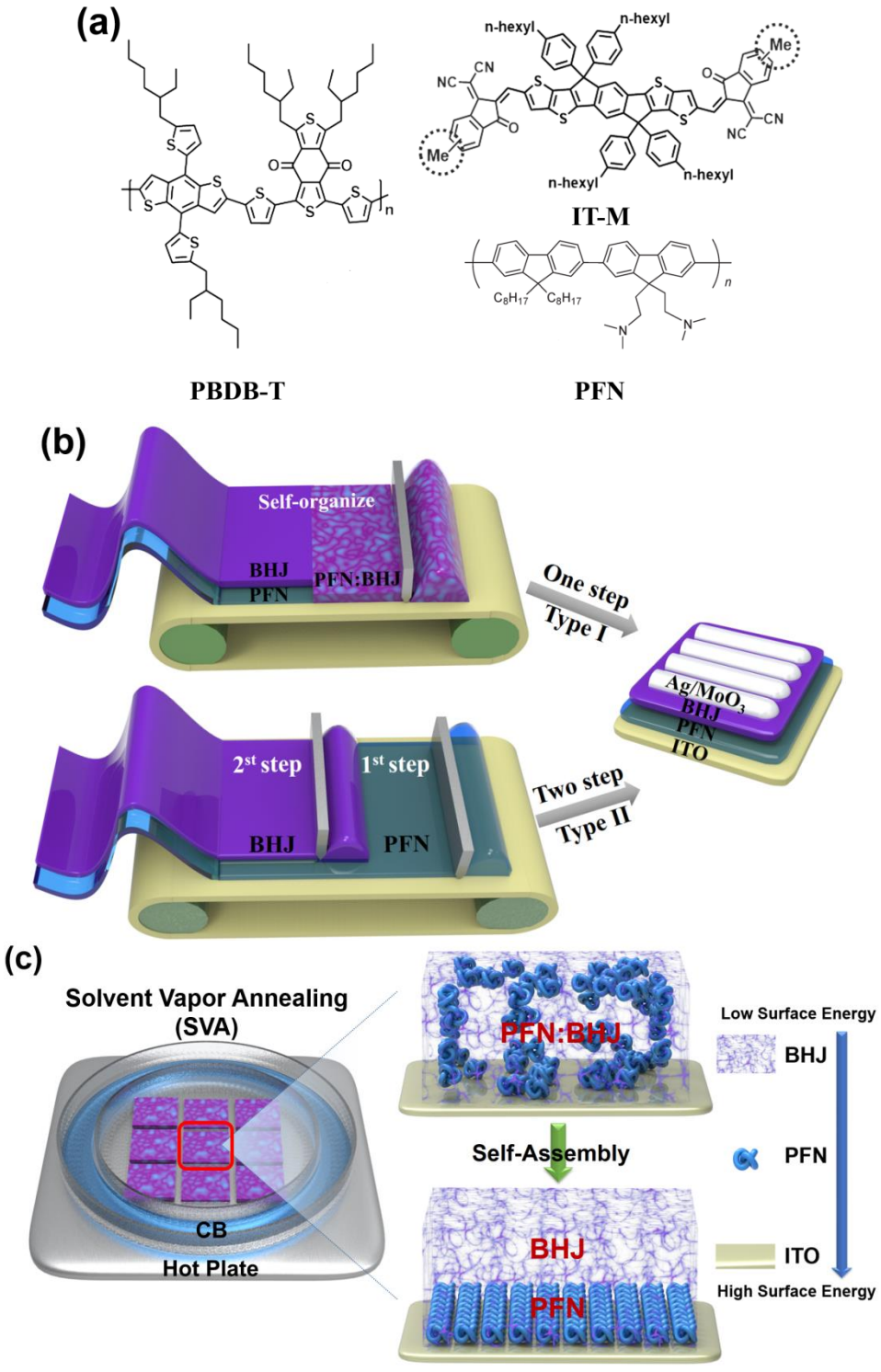

Figure 1. a) Chemical structures of PBDB-T, IT-M and PFN. b) The one-step and two-step doctor blading fabrication process and device architecture used in this study. c) The schematic diagram of SVA treatment and spontaneous PFN molecule segregation processed by SVA.

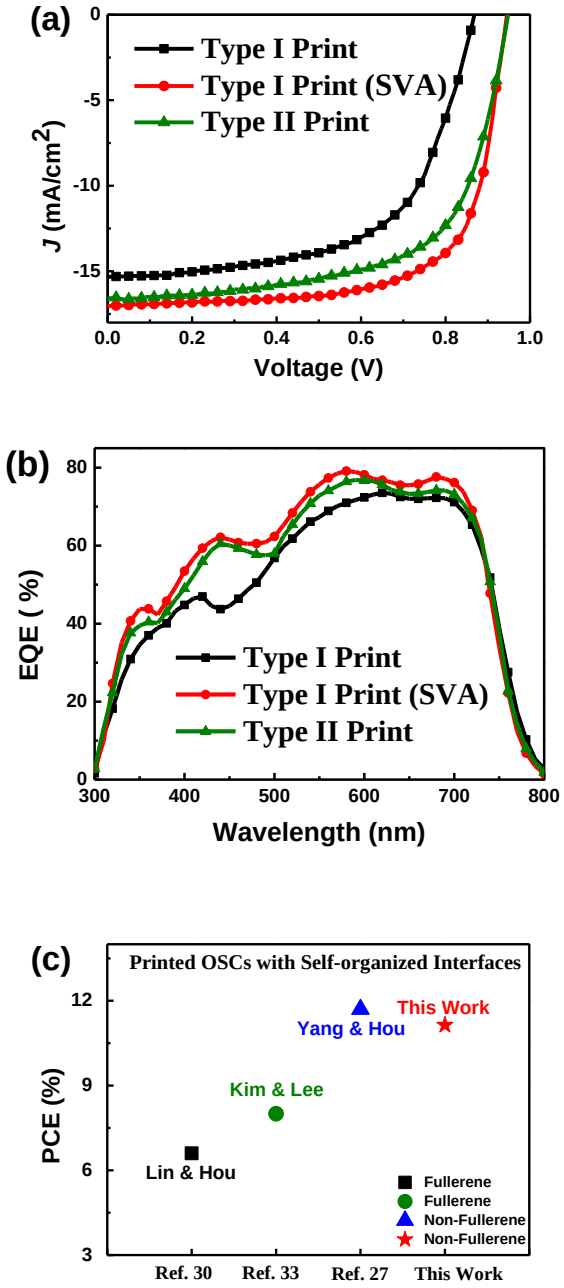

Figure 2. a) *J-V* curves of OSCs based on PBDB-T:IT-M with doctor blading method. b) EQE curves of OSCs based on PBDB-T:IT-M with doctor blading method. c) A comparison of the performance with previously reported single-junction OSCs with self-organized IL.

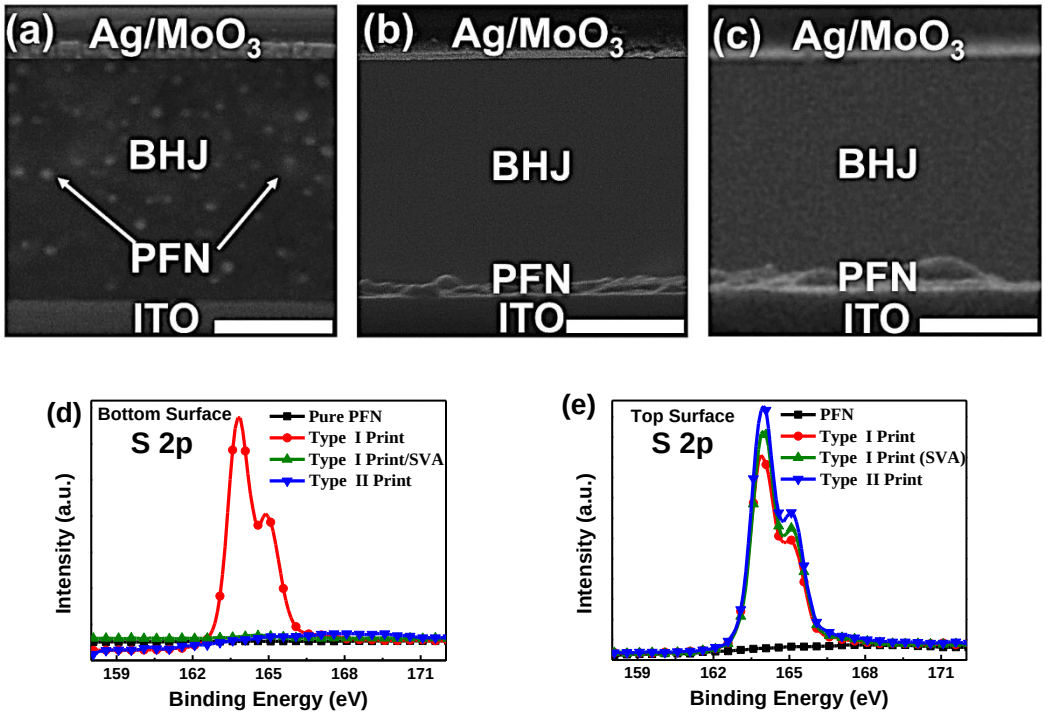

Figure 3. Cross-sectional SEM images of a) Type-I, b) Type-I (SVA) and c) Type-II active films (SEM bar =50 nm). Relative S 2p XPS spectra of d) bottom and e) top surfaces of various films.

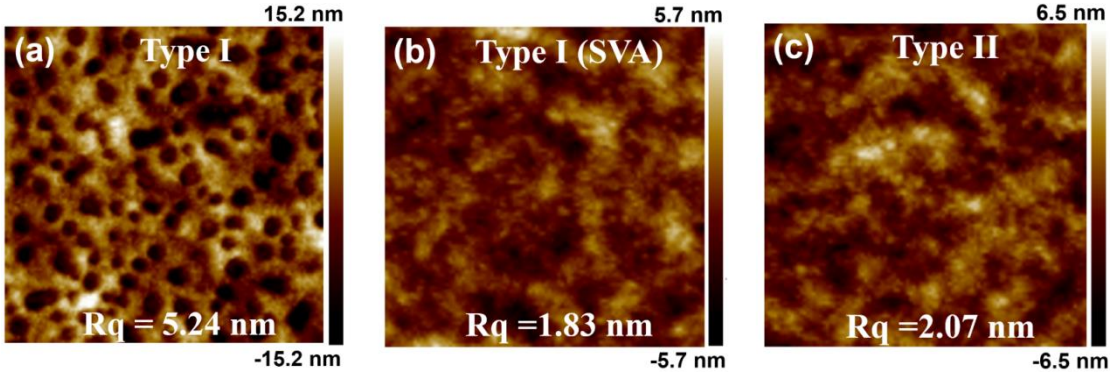

Figure 4. AFM height images of a) Type-I, b) Type-I (SVA) and c) Type-II (AFM image dimensions: 2 μm × 2 μm).

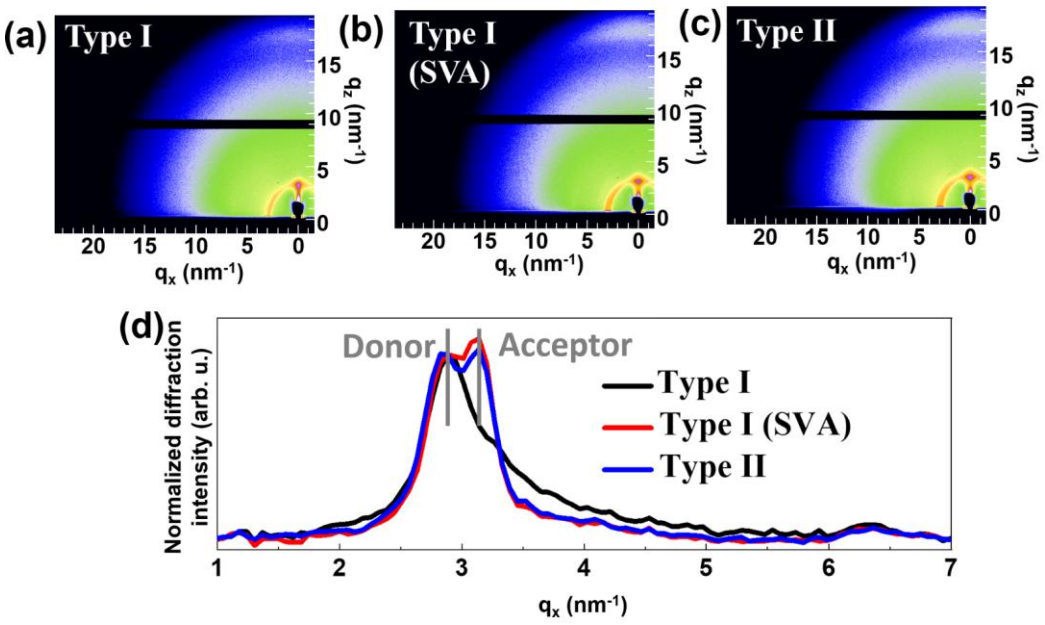

Figure 5. a-c) GIWAXS images of doctor-bladed films with Type I (print), Type I (print/SVA) and Type II (print/print). d) A plot displaying the diffraction intensity distribution along the horizon obtained by integrating in-plane cake slices from the GIWAXS images. (The curves are normalized to the diffraction intensity of the PBDB-T.)

Table 1. Solar cell parameters of PBDB-T:IT-M devices by doctor blading under illumination of AM 1.5G (100 mW/cm^2).

Method	Deposition conditions	J_{SC} [mA/cm^2]	V_{OC} [V]	FF	PCE_{max} [%]
One-step	Print[a]	15.32 (15.17)[b]	0.87	0.60	8.05 (7.65)[c]
	Print + SVA	17.05 (16.80)	0.94	0.69	11.14 (10.69)
Two-step	Print	16.58 (16.39)	0.94	0.64	10.06 (9.78)

[a]OSCs are deposited at 70 °C. [b]Data from EQE measurement. [c]Average PCE of 20 devices.

The fabrication of efficient organic solar cells via the combination of one-step doctor-blading and solvent vapor annealing (SVA), is reported for the first time. SVA improves the spontaneous stratification of the interlayer between the active layer and electrode. The achieved efficiency of 11.14% is among the highest reported to date for doctor-blade coated organic solar cells.

Keyword: one-step doctor blading; solvent vapor annealing; nonfullerence organic solar cell; self-assembly; interfacial layer

Yuanbao Lin, Liyang Yu, Yuxin Xia, Yuliar Firdaus, Sheng Dong, Christian Müller, Olle Inganäs, Fei Huang, Thomas D. Anthopoulos,* Fengling Zhang,* and Lintao Hou,*

One-step blade-coated highly efficient nonfullerene organic solar cells with a self-assembled interfacial layer enabled by solvent vapor annealing